Water distribution at solid/liquid interfaces visualized by frequency modulation atomic force microscopy

2010 Sci. Technol. Adv. Mater. 11 033003

(http://iopscience.iop.org/1468-6996/11/3/033003)

IOP PUBLISHING SCIENCE AND TECHNOLOGY OF ADVANCED MATERIALS

Sci. Technol. Adv. Mater. **11** (2010) 033003 (18pp) doi:10.1088/1468-6996/11/3/033003

TOPICAL REVIEW

Water distribution at solid/liquid interfaces visualized by frequency modulation atomic force microscopy

Takeshi Fukuma[1,2]

[1] Frontier Science Organization, Kanazawa University, Kakuma-machi, Kanazawa 920-1192, Japan
[2] PRESTO, Japan Science and Technology Agency, Honcho 4-1-9, Kawaguchi 332-0012, Japan

E-mail: fukuma@staff.kanazawa-u.ac.jp

Received 16 March 2010
Accepted for publication 3 June 2010
Published 8 September 2010
Online at stacks.iop.org/STAM/11/033003

Abstract
Interfacial phenomena at solid/water interfaces play an important role in a wide range of industrial technologies and biological processes. However, it has been a great challenge to directly probe the molecular-scale behavior of water at solid/water interfaces. Recently, there have been tremendous advancements in frequency modulation atomic force microscopy (FM-AFM), enabling its operation in liquids with atomic resolution. The high spatial and force resolutions of FM-AFM have enabled the visualization of one-dimensional (1D) profiles of the hydration force, two-dimensional (2D) images of hydration layers and three-dimensional (3D) images of the water distribution at solid/water interfaces. Here I present an overview of the recent advances in FM-AFM instrumentation and its applications to the study of solid/water interfaces.

Keywords: frequency modulation atomic force microscopy, lipid bilayer, hydration, atomic resolution imaging

1. Introduction

At solid/liquid interfaces, atoms and molecules constituting the solid surface interact with solvent or solute molecules, leading to the formation of molecular complexes or a non-uniform distribution of the mobile molecules. Such interfacial phenomena are important in various scientific and industrial fields such as electrochemistry, tribology, fluid mechanics and life science. Among the various interfacial phenomena, those at solid/water interfaces are of particular importance owing to their strong relevance to the human life. For example, the human body mostly consists of an aqueous solution, in which various biomolecules interact with water or other molecules at the interfaces between molecules and the physiological solution. Such interactions play an important role in biological processes.

At a solid/water interface, the influence of the solid surface on the properties of adjacent water molecules typically extends to a distance equivalent to a few water layers. As the size of a water molecule is approximately 0.2 nm, studies of solid/water interfaces are focused on physical phenomena at an interfacial space with a thickness of less than 1 nm and hence require subnanometer resolution.

So far, spectroscopic techniques such as x-ray reflectivity [1] and neutron diffraction [2] have been used for satisfying this requirement. These methods make it possible to measure the density profile of water molecules at a solid/water interface with molecular-scale resolution. Thus, they have been widely used as a powerful tool in studies of solid/water interfaces. However, the lateral resolution of such spectroscopic methods is low, typically on the order of micrometer. This problem is particularly serious in

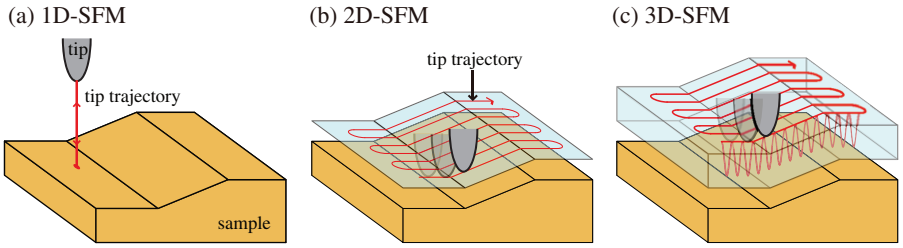

Figure 1. Schematic illustrations showing basic principles of (a) 1D-SFM, (b) 2D-SFM and (c) 3D-SFM. In 1D-SFM, the tip is scanned vertically. In 2D-SFM, the tip is scanned laterally and in 3D-SFM, the tip is scanned both laterally and vertically to probe the interfacial space. (Reproduced with permission from [4] © 2010 American Physical Society.)

studies of solid/water interfaces having a non-uniform lateral distribution, such as a biological membrane consisting of a complex mixture of various biomolecules.

Atomic force microscopy (AFM) [3] is measurement technique having a subnanometer spatial resolution in both the vertical and lateral directions. In this method, a cantilever with a sharp tip at its end is used as a force sensor. The radius of the tip is typically smaller than 10 nm. The tip is positioned near the sample surface to detect the interaction force acting on the tip (F_t). At solid/liquid interface, the tip interacts with surrounding solvent molecules and with the solid surface. Thus, the distribution of F_t measured at the solid/liquid interface shows a strong correlation with the distribution of solvent molecules.

To perform such a measurement at a solid/water interface, a piconewton force has to be detected with subnanometer resolution which can be achieved by frequency modulation AFM (FM-AFM) [5]. Although the method has traditionally been used in ultrahigh-vacuum environments, recent advances in FM–AFM [6] have enabled its operation in a liquid with subnanometer resolution [7, 8].

In FM-AFM, the cantilever is mechanically oscillated at its resonance frequency (f_0). As the tip approaches a surface, F_t induces a shift of the cantilever resonance frequency (Δf). The shift is recorded for either measuring F_t or controlling the vertical tip position with respect to the surface. To visualize water distribution at a solid/water interface, Δf values are recorded while the tip is scanned in an interfacial space. By scanning the tip in the vertical Z-direction, an F_t versus distance curve (force curve) is recorded as shown in figure 1(a). Such one-dimensional scanning force microscopy (1D-SFM) has been used for visualizing water distribution in the vertical direction. By scanning a tip in the XY-direction, i.e. parallel to the surface, a force image (constant-height mode) or a height image (constant-force mode) is obtained as shown in figure 1(b). Such two-dimensional scanning force microscopy (2D-SFM) is used for visualizing the lateral water distribution. These capabilities have been demonstrated by visualizing hydration layers formed at an interface between a model biological membrane and an aqueous solution [9].

Although the results obtained by 1D- and 2D-SFM provide valuable information that cannot be obtained by conventional techniques, they provide only a fraction of the information contained in a three-dimensional (3D) interfacial space. To resolve this issue, the author and his co-workers have recently developed a method referred to as

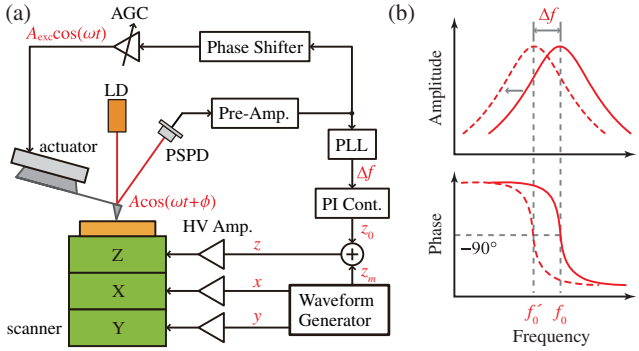

Figure 2. (a) FM–AFM setup. The vertical modulation signal (z_m) is used only in 3D-SFM. In 1D-SFM, the voltage signals for driving the lateral XY scanners (x and y) are used for locating the tip at a fixed XY position, and the dependence of Δf on the distance is measured. Hence, the values of x and y are fixed during force measurements. (b) Frequency dependences of the amplitude and phase plotted around f_0. The dotted and solid lines show the curves with and without F_t, respectively. Attractive and repulsive F_t induce negative and positive Δf, respectively.

three-dimensional scanning force microscopy (3D-SFM) [4]. In this method, the tip is scanned in both the Z and XY directions (figure 1(c)). Once a 3D force field is obtained, any 1D force profile or 2D force image can be extracted from it. In this way, water distribution at a solid/water interface can be investigated more efficiently and accurately than performing 1D- and 2D-SFM experiments. This advantage of 3D-SFM has been demonstrated by applying it to a mica/water interface, where 3D distributions of adsorbed water molecules and a hydration layer were visualized in a 3D force image with the atomic-scale resolution [4].

In this article, I overview the basic operation modes of FM-AFM, the development of FM-AFM instruments for liquid-environment operation and FM-AFM applications to solid/water interfaces.

2. Principles of FM-AFM

2.1. Force detection

Figure 2(a) shows a schematic of an FM-AFM setup. In FM-AFM, a microfabricated cantilever with a sharp tip at its end is used as a force sensor. The cantilever is mechanically oscillated at its resonance frequency (f_0) using

a piezoactuator. The cantilever vibration is detected by the optical beam deflection (OBD) method.

In the OBD method [10], a focused laser beam irradiates the backside of the cantilever and the reflected beam is detected using a position-sensitive photodetector (PSPD). A two- or four-element Si p-i-n photodiode is typically used as the PSPD, and hereafter a two-element photodiode is assumed. The photoinduced currents from the photodiode elements are fed into a preamplifier. There, current-to-voltage (*IV*) converters convert the currents to the voltages. The two voltage signals from the *IV* converters are fed into a differential amplifier, which outputs the difference between the two input signals.

Before the tip approaches the surface, the position of the PSPD is adjusted so that the laser spot on the PSPD is located at the boundary between the two photodiode elements. Changes in the vertical position of the tip (z_t) displace the cantilever, and thus the laser beam is reflected from the cantilever backside to the PSPD. The boundary between the two photodiode elements is oriented perpendicularly to the direction of the laser spot displacement so that it induces a difference between the two photoinduced currents. As a result, the output of the differential amplifier changes in proportion to the cantilever deflection and hence is referred to as deflection signal.

The cantilever vibration induced by the piezoactuator is detected as the ac component of the deflection signal. The deflection signal is routed back to the piezoactuator through a phase shifter and an automatic gain control (AGC) circuit to form a self-oscillation loop as shown in figure 2(a). In this self-oscillation loop, the cantilever acts as a mechanical resonator so that the cantilever oscillation frequency (f) is maintained at the resonance frequency of the cantilever.

Here I explain this mechanism with the frequency dependences of the amplitude and phase around f_0 shown in figure 2(b). The phase difference (ϕ) between the cantilever excitation signal and the deflection signal becomes -90° at the cantilever resonance. In the steady state, the total phase delay of the self-oscillation loop is equal to a multiple of 360°. If the phase delay at the phase shifter is adjusted so that $\phi = -90^\circ$, then the cantilever always oscillates at a frequency at which ϕ equals -90°, namely, at the resonance frequency. The AGC circuit adjusts the cantilever excitation amplitude (A_{exc}) to maintain a constant cantilever oscillation amplitude (A).

Owing to the self-oscillation loop, Δf can be measured by detecting the frequency change of the deflection signal. For this purpose, the deflection signal is fed into a frequency detector, which outputs a voltage signal proportional to Δf. A phase-locked loop (PLL) circuit is typically used as the frequency detector.

If the cantilever oscillation amplitude is sufficiently small to assume that the force gradient ($\partial F_t/\partial z_t$) in the Z range of cantilever oscillation is constant, then Δf is proportional to the force gradient and is given by [5]

$$\Delta f(z_t) = \frac{f_0}{2k}\frac{\partial F_t(z_t)}{\partial z_t}, \tag{1}$$

where k denotes the spring constant of the cantilever. For an arbitrary oscillation amplitude, this relationship is given by [11]

$$\Delta f(z_t) = \frac{f_0}{2k}\int_{-A}^{A}\frac{\partial F_t(z_t+q)}{\partial z_t}\frac{\sqrt{A^2-q^2}}{\pi A^2/2}\mathrm{d}q. \tag{2}$$

In this equation, the force gradient multiplied by the weight function is integrated over the Z range of cantilever oscillation. For a large oscillation amplitude, the derivative of $F_t(z_t)$ is integrated over a large z_t range. Consequently, Δf is almost proportional to F_t.

2.2. 1D-SFM

In 1D-SFM, the tip is fixed laterally and scanned in the Z-direction as shown in figure 1(a). The Z scan is performed by applying a triangular wave to the Z scanner. During the approach and retraction, values of Δf are recorded. The measured values are plotted as a function of z_t to obtain a Δf versus distance curve.

The obtained Δf versus distance curve can be converted to a quantitative F_t versus distance curve using the following equation [12].

$$F_t(z_t) = \frac{2k}{f_0}\int_{z_t}^{\infty}\left(1+\frac{a^{1/2}}{8\sqrt{\pi(q-z_t)}}\right)\Delta f(q) - \frac{a^{3/2}}{\sqrt{2(q-z_t)}}\frac{\mathrm{d}(\Delta f(q))}{\mathrm{d}q}\mathrm{d}q. \tag{3}$$

This equation is valid for an arbitrary oscillation amplitude and has been widely used. However, it has a few important limitations [13]. The Δf versus distance curve must include a Z distance range with no variations of Δf. Namely, the Δf curve must be taken from a sufficiently large Z distance to avoid the effect of the solid surface. Another limitation is that F_t must be a unique function of the absolute Z position of the tip. Note that the 'absolute position' is not equal to the averaged Z position but includes the displacement due to cantilever oscillation. For example, if a bond is created and broken at different Z positions (which occurs in adhesion measurements, unfolding force measurements and ligand–receptor interaction measurements), then the values of F_t in the approach and retraction processes are different, and hence the force conversion formula does not give a correct value. These limitations should be taken into account when the equation is used for force conversion.

2.3. 2D-SFM

In 2D-SFM, z_t is controlled to maintain Δf at the preset value (Δf_{sp}) as shown in figure 1(b). The Z distance is regulated by a proportional-integral (PI) controller, as shown in figure 2(a). The Δf signal is fed into the PI controller, which outputs a Z control signal (z_0) to maintain the values of Δf at Δf_{sp}. The XY scan is performed by applying a triangular wave to the X scanner and a ramp signal to the Y scanner. During the XY scan, values of z_0 are recorded to obtain a 2D height image.

Note that the image obtained by 2D-SFM does not necessarily represent the true surface corrugations. Strictly speaking, the image shows a constant-Δf surface. If Δf versus distance curves measured at any XY position show a similar profile, then this difference is negligible. For nanoscale 2D-SFM imaging, a major difference originates from any inhomogeneity in surface properties, and for atomic-scale 2D-SFM imaging it originates from any inhomogeneity in the properties of underlying atoms or molecules. Therefore, an accurate interpretation of atomic-scale contrasts in a 2D-SFM image generally requires a detailed comparison with the results of a theoretical simulation.

Another problem is that a 2D-SFM image cannot be directly converted to a quantitative force image. By taking a force curve at an arbitrary XY position and converting it to a quantitative force curve, one can estimate the force corresponding to Δf_{sp}. However, this method is valid only when one can assume that the force versus distance curves measured at any XY position show a similar profile. If this assumption is not satisfied, a Δf versus distance curve should be collected at every XY position and converted to a quantitative force curve. This is possible by obtaining a 3D Δf image by 3D-SFM as described below.

2.4. 3D-SFM

In 3D-SFM, a tip is scanned in both the Z and XY directions to measure F_{t} in the whole 3D interfacial space (figure 1(c)). The major difference between the setups for 2D- and 3D-SFM is the use of a Z modulation signal (z_m) in 3D-SFM as shown in figure 2(a); z_t is modulated with a sine wave faster than the bandwidth of the Z feedback control while the tip is laterally scanned. During the scan, Δf is recorded in real time with respect to the 3D tip positions while the average tip height (z_0) is regulated to maintain a constant average value of Δf. As the tip motion induced by the Z modulation is faster than the bandwidth of the Z feedback control, the Z modulation induces repeated cycles of the tip approach and retraction. The variations of Δf induced by the Z scan are recorded in real time to produce a pair of Δf versus distance curves for approach and retraction in each cycle. A 3D Δf image is constructed from either approaching or retracting Z profiles at each XY position. A quantitative 3D force image is obtained by applying the force conversion formula (equation (3)) to the individual Z profiles constituting the 3D Δf image. Although there are no limitations on the amplitude of z_m, it is typically set to less than a few nanometers, which corresponds to a typical value for the vertical extent of the interfacial space.

Previously reported 3D imaging techniques using SFM were developed on the basis of 1D spectroscopy [14] or 2D constant-height imaging [15–17], and hence have no tip–sample distance regulation during the measurement. In addition, owing to the complex tip motion, measurement by these techniques takes hours or even days. Therefore, it has been difficult to use these techniques in a liquid at room temperature without the tip crashing or image distortion caused by tip drift. In contrast, 3D-SFM is based on 2D constant-Δf imaging, and hence has Z feedback control during the tip scan. In addition, the simple motion of the tip dramatically reduces the measurement time, allowing this technique to even be applied to liquids.

3. Instrumentation of FM-AFM

The FM-AFM setup consists of various components as shown in figure 2(a). Although most of them are commonly used in all operating environments, special requirements are imposed on the design of the cantilever excitation mechanism and the cantilever deflection sensor for operation in a liquid. The rest of this section describes these special requirements and the proposed design concepts.

3.1. Spurious-free cantilever excitation

3.1.1. Requirements of stability and accuracy. In FM-AFM, the cantilever is mechanically oscillated at its resonance frequency using a self-oscillation circuit. The self-oscillation circuit acts as a feedback circuit, which controls the cantilever excitation frequency so that ϕ is maintained at -90°. This feedback control is based on the assumption that ϕ monotonically decreases with increasing f as shown in figure 2(b). Thus, a strong distortion of the phase curve can hinder stable self-oscillation. In addition, if the slope of the phase curve deviates from the true cantilever characteristics, the relationship between Δf and F_{t} also deviates from equations (2) and (3), hindering quantitative force measurements by FM-AFM. Therefore, stable and accurate force measurements by FM-AFM require a spurious-free cantilever excitation mechanism to allow the measurement of an ideal phase versus frequency curve.

The excitation of the cantilever is typically performed by applying an ac voltage to a piezoactuator placed close to the cantilever (piezoelectric excitation [18]). In this method, the acoustic wave generated by the piezoactuator is transmitted to all the components mechanically coupled with the piezoactuator. If any mechanical resonance around f_0 exists in the transmission path of the acoustic wave, the vibration of such a spurious resonance is excited. While this vibration itself may affect the deflection signal and give rise to a distortion in the phase curve, it also induces the phase delay of the acoustic wave transmitted to the cantilever. Consequently, the transfer function of the acoustic wave from the piezoactuator to the cantilever is influenced by spurious resonances, leading to a distortion in the phase curve.

The ideal phase versus frequency curve is given by

$$\phi(f) = \tan^{-1}\left\{\frac{1}{Q(f/f_0 - f_0/f)}\right\}. \tag{4}$$

Assuming $\Delta f \ll f_0$ and $\phi \simeq -90^\circ$ the slope of the phase curve is given by,

$$\frac{\partial \phi}{\partial f} = -\frac{2Q}{f_0}. \tag{5}$$

This equation shows that the slope is approximately proportional to the quality factor Q. Thus, the high Q factor in

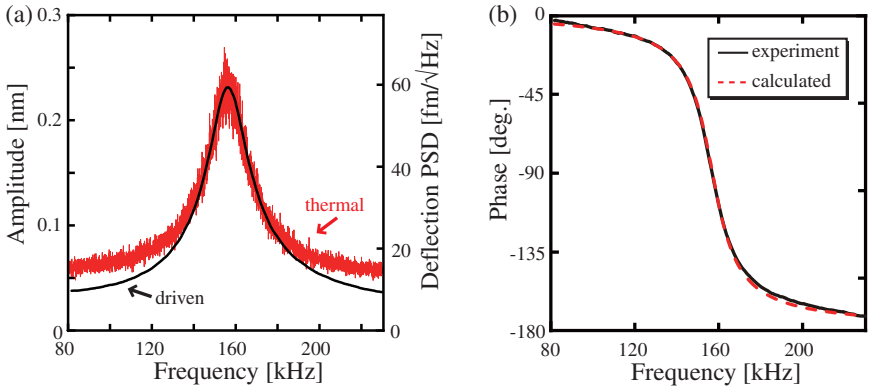

Figure 3. Frequency dependences of (a) amplitude and (b) phase measured by photothermal excitation in water [21]. The power spectral density (PSD) spectrum of the deflection signal measured without cantilever excitation is superposed on the amplitude curve obtained using the driven cantilever in (a). The values of Q and f_0 obtained by fitting the thermal PSD spectrum with equation (6) are 8.7 and 157.079 kHz, respectively. The dotted line in (b) is calculated using these parameters and equation (4) while the solid line shows experimental values. (Reproduced with permission from [21] © 2009 American Institute of Physics.)

vacuum ($Q = 10\,000 - 100\,000$) provides a large phase slope while the low Q factor in a liquid ($Q = 1$–10) results in a small phase slope. This difference makes it difficult to avoid the distortion of the phase curve in a liquid.

As the Q factor of the spurious resonance (Q_s) is much smaller than that of the cantilever resonance in vacuum, the frequency dependence of the phase delay caused by the spurious resonance is negligible compared with the strong frequency dependence of the phase of the cantilever vibration. In contrast, the Q factor in a liquid is often smaller than Q_s so that the phase delay caused by the spurious resonance is not negligible. In addition, in the case of liquid-environment AFM, the cantilever holder is in contact with the liquid, through which the acoustic wave is transmitted to the sample holder. Thus, spurious resonances in these additional components can also affect the phase curve.

To reduce or eliminate the influence of such spurious resonances, several designs have been proposed for spurious-free cantilever excitation, including magnetic [19], photothermal [20] and improved piezoelectric excitation [21]. The rest of this section describes the basic principles of these designs and the practical issues in their application.

3.1.2. Magnetic excitation. In the case of magnetic excitation [19], the cantilever is coated with a magnetic thin film or a magnetic bead is attached on the backside of the cantilever. An ac magnetic field is generated with a coil placed below the sample or above the cantilever. Owing to the ac magnetic field, an ac magnetic force is applied directly to the cantilever. In this way, ideal amplitude and phase versus frequency curves are obtained even in a liquid.

Several issues must be taken into account in magnetic excitation. To attach a magnetic bead, the cantilever must be relatively large, which may limit the range of cantilevers compatible with this method. The attachment of a magnetic bead increases the mass of the cantilever and thus decreases its resonance frequency. The impedance of a coil increases with increasing driving frequency. Thus, it becomes more difficult to drive the cantilever as the cantilever resonance frequency increases. When the magnetic film is coated by sputtering, the tip apex is often covered with a thin magnetic film. This increases the tip radius, leading to low spatial resolution or instability. The magnetic materials are not necessarily passive to the liquid used in AFM experiments and hence may dissolve and contaminate the sample.

3.1.3. Photothermal excitation. In the case of photothermal excitation [20], the cantilever is coated with a thin film of gold. A laser beam with a power modulated at the cantilever driving frequency (f) irradiates the backside of the cantilever and induces thermal expansion of the gold film and cantilever body. Owing to the difference in their thermal expansion coefficients, a mechanical stress is generated at the film/cantilever interface, which gives rise to a driving force synchronized with the laser power modulation. In this way, the cantilever is directly driven by the laser beam.

Figure 3 shows the frequency dependences of the amplitude and phase measured by photothermal excitation in water [21]. The PSD of the cantilever deflection signal measured without cantilever excitation (n_{zB}) is also shown in figure 3(a). This PSD spectrum corresponds to the cantilever vibration induced by the thermal energy, which is given by [5]

$$n_{zB} = \sqrt{\frac{2k_B T}{\pi f_0 k Q} \frac{1}{[1-(f/f_0)^2]^2 + [f/(f_0 Q)]^2}}, \qquad (6)$$

where k_B and T denote Boltzmann's constant and absolute temperature, respectively. By fitting the PSD spectrum with this equation, the correct values of Q and f_0 are deduced. Using these values and equation (4), an ideal phase curve is obtained as indicated by a dotted line in figure 3(b). The amplitude and phase curves obtained by photothermal excitation show good agreement with the ideal cantilever characteristics described by equations (6) and (4), respectively. This ensures stable and accurate force measurements in liquids by FM-AFM.

There are several practical issues in photothermal excitation. The cantilever must be coated with a thin film of gold. Although gold is chemically inert, a thin Cr film is often used as an adhesion layer, which may dissolve in some solutions and contaminate the sample. As an alternative to Cr, Ti may be used to improve the chemical resistivity. If the gold film is deposited by sputtering, the tip apex is likely to be covered with gold. The deposited gold increases the tip radius and hence reduces the spatial resolution. Coating an Au/Ti thin film by electron beam deposition in high vacuum may be a solution to this problem.

Another issue is the influence of the laser beam. Laser irradiation, particularly in the UV range, can modify the sample. An infrared (IR) laser beam is less likely to modify the sample, but is mostly reflected by gold owing to the high reflectivity of gold in the near IR-range. Thus, a relatively high power is used, which may heat the cantilever, sample or solution. To avoid heating, it is important to reduce the laser power during the laser alignment to the cantilever backside. In addition, the laser spot should be smaller than the cantilever.

3.1.4. Improved piezoelectric excitation. In spite of the distortions in the amplitude and phase curves, piezoelectric excitation has been the most widely used method even for liquid-environment AFM. This is mainly due to its simplicity and wide applicability. The method requires no modifications to the cantilever and is hence compatible with all commercially available cantilevers. Thus, there has been strong demand for improving the performance of piezoelectric excitation.

Because spurious resonances are induced by an acoustic wave in piezoelectric excitation, considerable efforts have been made to control its propagation from the piezoactuator to the cantilever. For example, Degertekin *et al* proposed the use of an ultrasonic wave [22, 23]. Owing to the short wavelength of an ultrasonic wave, its propagation path can be controlled using a Fresnel lens. By modulating the amplitude of the ultrasonic wave, the cantilever can be driven at an arbitrary frequency. Carrasco *et al* presented a cantilever holder design with an acoustic absorber [24]. There, a piezoactuator is placed close to the cantilever and an acoustic absorber is placed in the propagation path from the piezoactuator to the other mechanical components to prevent the excitation of spurious resonances.

In contrast to these ideas, the author and his co-workers recently presented a different design concept [25]. Instead of an acoustic wave, the cantilever is driven using the elastic deformation of a flexure hinge (flexure drive mechanism). Figure 4 shows the two-dimensional distribution of vibration amplitude in a simplified model of a flexure hinge made of metal (stainless steel SS316) or plastic (polyether ether ketone, PEEK) simulated by the finite element method. The hinge made of a compliant material (PEEK) exhibits a large elastic deformation, whereas the one made of a rigid metal (SS316) shows almost no deformation. The amplitude and phase curves obtained with a PEEK holder are markedly superior to those obtained with an SS316 holder.

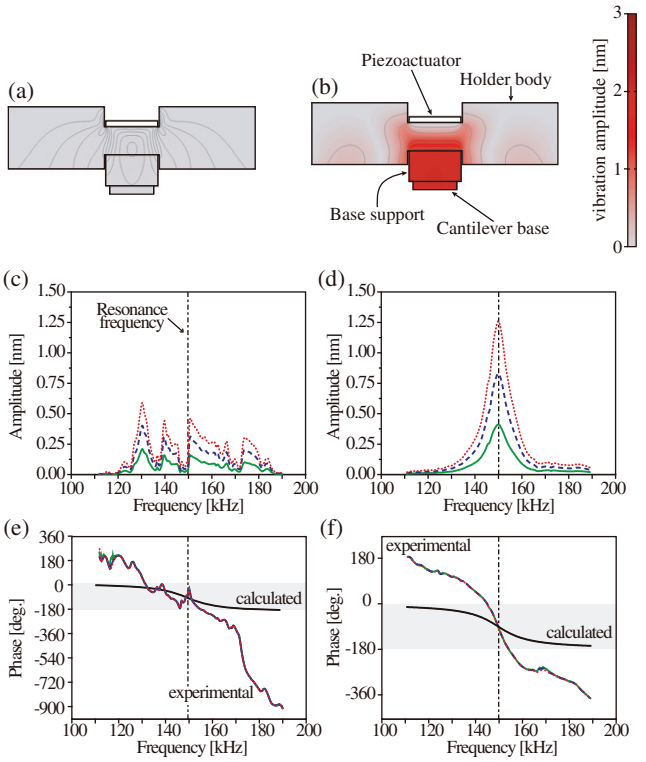

Figure 4. Two-dimensional distribution of vibration amplitude in a simplified model of a flexure hinge made of (a) SS316 and (b) PEEK simulated with the finite element method. Also shown are the frequency dependences of the amplitude and phase obtained in water using the cantilever holder with the holder body made of SS316 ((c) and (e)) and PEEK ((d) and (f)). The cantilever was driven by an excitation signal with an amplitude of 50, 100 or 150 mV. Note that the measured phase curves in (e) and (f) appear as a single curve owing to their weak dependence on the excitation amplitude. (Reproduced with permission from [25] © 2009 American Institute of Physics.)

The distinctive advantage of this design is that the amplitude and phase characteristics are improved without deteriorating the advantages of the piezoactuator, i.e. simplicity and usability. The method does not require any special devices such as a coil, an additional laser diode, an ultrasonic transducer or a Fresnel lens. In addition, the piezoactuator is completely isolated from the liquid, which eliminates the need for coating the piezoactuator with an insulating material.

The amplitude response obtained by the flexure drive mechanism shows a clean peak at the true resonance frequency of the cantilever estimated from the thermal vibration spectrum. In contrast, the phase curve deviates from the ideal response. This is due to the additional frequency-dependent phase delay caused by the finite response time of the elastic deformation. However, the important difference between the phase curves in figures 4(e) and (f) is the linearity. If the erroneous phase delay induced by the driving mechanism of the cantilever or a spurious resonance has a linear frequency dependence, there is a way to recover the force value.

From the slope of the measured phase curve, an apparent Q factor (Q_a) is obtained with equation (5). The apparent

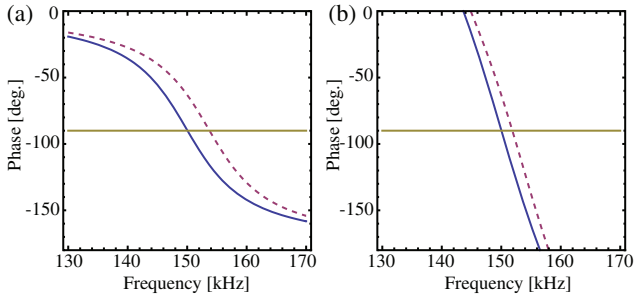

Figure 5. Phase versus frequency curves ($k = 40$, $Q = 10$, $f_0 = 150$ kHz). (a) True cantilever response calculated with equation (4). (b) Apparent cantilever response ($Q_a = 20$) with an artificial phase delay calculated with equation (7). The dotted and solid lines respectively show phase curves with and without an external force gradient of 2 N m^{-1}.

phase curve measured around the resonance frequency is given by

$$\phi_a(f) \equiv -\frac{2Q_a}{f_0}(f - f_0) = \phi(f) - \frac{2\Delta Q}{f_0}(f - f_0), \qquad (7)$$

where ΔQ is the difference between the apparent and true Q factors (i.e. $\Delta Q \equiv Q_a - Q$). The first term of the right-hand side of this equation changes with F_t, while the second term is independent of F_t. Thus, the measured Δf does not match the value expected from equation (2). Figure 5 shows the true and apparent phase curves obtained with and without an external force gradient. Because of the erroneous phase delay, the phase curve in figure 5(b) shows a smaller frequency shift than that in figure 5(a).

The true Δf value can be recovered by multiplying by a correction factor χ_f given by

$$\chi_f = \frac{Q_a}{Q}. \qquad (8)$$

In the example shown in figure 5(b), $\chi_f = 2$. In fact, the frequency shift at the -90° phase shift in figure 5(a) is twice as large as the value in figure 5(b).

Note that the erroneous phase delay may not be constant. If the phase delay is partially caused by a spurious resonance induced by an acoustic wave transmitted through the liquid, it can change upon evaporation of the liquid. Thus, the apparent phase slope should be measured immediately before or after the measurement. Another limitation is that f_0 must be lower than the resonance frequency of the flexure hinge. In the design presented in [25], the resonance frequency of the flexure hinge is a few hundred kilohertz, which is larger than typical values for f_0 in a liquid. However, if a cantilever with a high f_0 becomes available in the future, it may limit the range of cantilevers compatible with this excitation method.

3.2. Low-noise cantilever deflection sensor

3.2.1. Requirements for atomic resolution. The recent progress of liquid-environment FM-AFM was triggered by the development of a low-noise OBD sensor in 2005 [6].

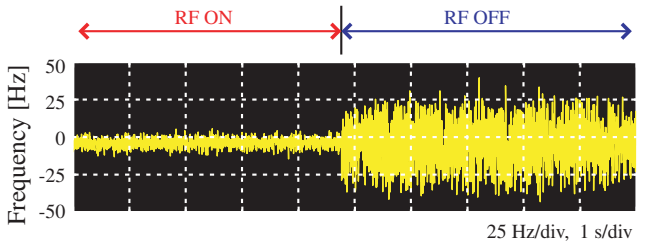

Figure 6. Waveform of the frequency shift signal measured in water before and after turning off the RF laser power modulation ($A = 5$ nm, $f_0 = 140$ kHz, $k = 42$ N m^{-1}). (Reproduced with permission from [6] © 2005 American Institute of Physics.)

Before this development, the deflection noise density arising from the cantilever deflection sensor (n_{zs}) was typically 100–1000 fm $\sqrt{\text{Hz}}^{-1}$. This noise level was reduced to 40 fm $\sqrt{\text{Hz}}^{-1}$ in liquid in 2005. The performance of the OBD sensor was further improved to give n_{zs} values of 7.3 fm $\sqrt{\text{Hz}}^{-1}$ in 2006 [26] and 4.7 fm $\sqrt{\text{Hz}}^{-1}$ in 2009 [21].

The development of the low-noise cantilever deflection sensor in 2005 had a strong impact on the AFM research field [6]. However, this was not necessarily because of the difficulty of the development itself. It was unexpected that the reduction of deflection sensor noise would result in such a large improvement in the FM-AFM performance. At that time, it was often postulated that the FM-AFM performance in liquid would be limited by the low Q factor of the cantilever. However, it has not been proven theoretically or experimentally that the noise from the instruments is small enough to achieve the optimal performance limited only by the Q factor.

The author carried out detailed noise analyses of all the components in the FM-AFM setup, compared the results with theoretical expectations and finally found that n_{zs} was too large to achieve the optimal FM-AFM performance in liquid. To understand the necessity of the low-noise cantilever deflection sensor, the necessity of a stiff cantilever and small oscillation amplitude should also be understood. Here I explain the necessity of these three factors for achieving true atomic resolution with FM-AFM in liquid.

The performance of FM-AFM is ultimately limited by the deflection noise arising from the thermal vibration of the cantilever. The PSD spectrum of the thermal vibration is given by equation (6). To achieve this optimal performance, n_{zs} must be reduced to a value less than n_{zB}. The noise components which influence the FM-AFM performance lie in the frequency range from $f_0 - B$ to $f_0 + B$, where B is the bandwidth of the measurement. The bandwidth B is typically within 1 kHz, which is smaller than the peak width of the PSD spectrum of the thermal vibration of the cantilever in liquid. Therefore, the condition $n_{zs} < n_{zB}$ is effectively the same as $n_{zs} < n_{zB}(f_0)$. From equation (6), the peak value for n_{zB} is given by

$$n_{zB}(f_0) = \sqrt{\frac{2k_B T Q}{\pi f_0 k}}. \qquad (9)$$

For a typical soft cantilever with $k = 0.1\,\mathrm{N\,m^{-1}}$, $f_0 = 5\,\mathrm{kHz}$ and $Q = 1.5$, the peak value is $n_{zB}(f_0) = 2800\,\mathrm{fm}\,\sqrt{\mathrm{Hz}}^{-1}$, which is larger than the n_{zs} values for a conventional deflection sensor. For a typical stiff cantilever with $k = 30\,\mathrm{N\,m^{-1}}$, $f_0 = 130\,\mathrm{kHz}$ and $Q = 8$, the peak value is $n_{zB}(f_0) = 74\,\mathrm{fm}\,\sqrt{\mathrm{Hz}}^{-1}$, which is smaller than the n_{zs} values for a conventional deflection sensor. Therefore, a low-noise cantilever deflection sensor is necessary to achieve the optimal performance in liquid with a stiff cantilever.

A stiff cantilever is required for two major reasons. Firstly, a soft cantilever has a large thermal vibration amplitude, which limits the precision in the control of the vertical tip position. The root-mean-square (RMS) amplitude of the cantilever thermal vibration $\langle z_{\mathrm{th}}\rangle$ is given by

$$\langle z_{\mathrm{th}}\rangle = \sqrt{\frac{k_{\mathrm{B}}T}{k}}. \tag{10}$$

For cantilevers with $k = 0.04$ and $40\,\mathrm{N\,m^{-1}}$, $\langle z_{\mathrm{th}}\rangle = 100$ and 10 pm, respectively. The height of atomic-scale corrugations in FM-AFM images ranges from 10 to 100 pm. Thus, the use of a stiff cantilever is necessary to achieve true atomic resolution. Note that it is possible to control the vertical position of the cantilever base with a precision better than 10 pm, even with a soft cantilever. However, as the cantilever itself shows uncontrolled vibration with an amplitude larger than 100 pm, it is impossible to regulate the position of the tip apex atom with atomic-scale precision.

Another reason for using a stiff cantilever is the stability. In an aqueous environment, long-range attractive forces such as van der Waals and electrostatic forces are mostly screened by water. However, owing to the short-range attractive forces caused by the hydration layers and hydrophobic interactions, their gradient often exceeds the spring constant (k) of the cantilever, leading to an adhesion event known as 'jump-to-contact'. To avoid such an instability, k has to be large enough to satisfy the following condition

$$k > \left|\frac{\partial F_{\mathrm{t}}}{\partial z_{\mathrm{t}}}\right|. \tag{11}$$

For static-mode AFM, this is the absolute condition that must be satisfied to avoid instability. In contrast, there is an alternative solution in dynamic-mode AFM, which is the use of a large oscillation amplitude (A). The restoring force of the cantilever at the tip position closest to the surface increases in proportion to A. If A is large enough to provide a restoring force larger than the adhesion force F_{ad}, the tip can be detached from the surface. This condition is given by

$$kA > F_{\mathrm{ad}}. \tag{12}$$

However, the use of a large amplitude reduces the sensitivity to short-range forces and increases the sensitivity to long-range forces, leading to a low spatial resolution. In addition, Giessibl *et al* reported that the optimal amplitude for providing the best signal-to-noise ratio (SNR) in force detection roughly corresponds to the decay length of the force component [27]. For obtaining an atomic-scale resolution, short-range force components having a decay length of a few angstroms have to be detected. Therefore, the optimal amplitude for obtaining an atomic resolution is a few angstroms. To avoid tip instability at a small oscillation amplitude, it is necessary to use a stiff cantilever.

In summary, to achieve true atomic resolution, the tip has to be controlled with atomic-scale precision. This requires a stiff cantilever oscillating with a small amplitude. To achieve the theoretically limited noise performance in FM-AFM under these conditions, a low-noise cantilever deflection sensor is necessary.

The use of a quartz-based force sensor known as a 'qPlus sensor' [28] may become an alternative in the future. The sensor has a higher k value (typically $1800\,\mathrm{N\,m^{-1}}$) and hence a smaller thermal vibration than a typical cantilever. In addition, its Q factor in liquid is expected to be much higher than usual due to the large mass. At present, owing to the low f_0 (typically 20–30 kHz) and the high k values, the force sensitivity obtained with this sensor is not likely to exceed the value obtained with a typical cantilever in liquid, which may limit the overall performance of FM-AFM. However, this demerit may be overcome in the future by enhancing f_0.

3.2.2. Low-noise OBD sensor. Among the various types of deflection sensors proposed so far, the OBD sensor has been used the most widely owing to its simple setup and easy optical beam alignment. The principle of the OBD method is explained in section 2.1.

Major noise sources in the OBD method include the Johnson noise from the transimpedance resistor in the IV converter, the shot noise from the PSPD and the optical feedback and interference noises induced by the laser beam. Although the ultimate limit of the performance is given by the shot noise, the optical feedback and interference noises are predominant in most OBD sensors, particularly in the case of liquid-environment AFM.

Such optical noises are greatly suppressed by modulating the laser power at a frequency from 300 to 500 MHz. The radio frequency (RF) modulation alters the laser emission from the single mode to the multimode. As the optical feedback noise arises from the competition between the different laser modes, the multimode laser operation greatly reduces mode hopping and hence the optical feedback noise.

The optical interference noise arises from the interference at the PSPD surface between the laser beam reflected at the backside of the cantilever and the laser beam reflected or scattered at the glass/air or glass/liquid interface (figure 7(a)). Such interference takes place if the coherence length of the laser beam (ℓ_{ch}) is longer than the difference between the optical paths of these two laser beams ($\Delta\ell$). To prevent this interference, ℓ_{ch} is reduced by RF modulation and $\Delta\ell$ is increased by placing an optical window relatively far from the cantilever backside (figure 7(b)). With these improvements, the laser noise is reduced to a value smaller than the noise from the PSPD shot noise.

The performance of the OBD sensor is ultimately limited by the PSPD shot noise. The PSD spectrum of the deflection

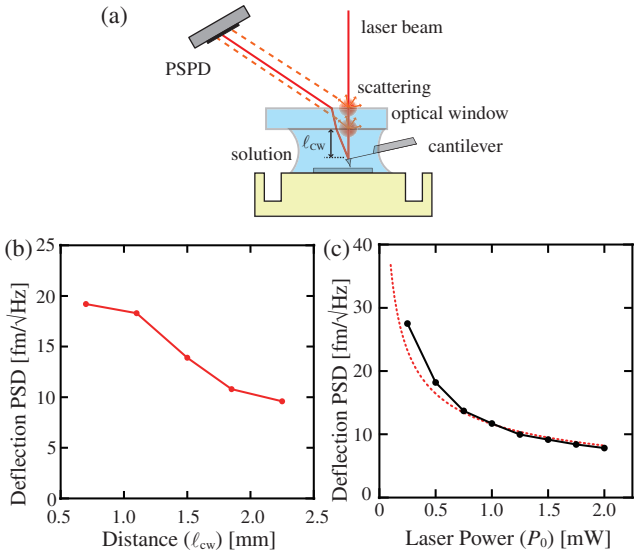

Figure 7. (a) Schematic illustration of the OBD sensor showing laser beam interference at the PSPD surface caused by scattering at the air/glass and glass/liquid interfaces. (b) Dependence of n_{zs} on the distance between the optical window and the cantilever backside (ℓ_{cw}). (c) Laser power (P_0) dependence of n_{zs}. (Reproduced with permission from [21] © 2009 American Institute of Physics.)

noise arising from the PSPD shot noise (n_{zp}) is given by [26]

$$n_{zp} = \frac{a_0 \ell_c}{6\chi n_m \ell_f} \sqrt{\frac{2e}{\eta \alpha P_0}}, \tag{13}$$

where a_0, χ, ℓ_f, e, η, α, ℓ_c and n_m are the diameter of the collimated laser beam, the correction factor for a Gaussian laser beam profile, the focal length of the focusing lens, the elementary charge, the efficiency of light-to-current conversion at the PSPD, the efficiency of optical transmission from the focusing lens to the PSPD, the cantilever length and the refractive index of the environment, respectively.

To obtain the shot-noise-limited performance described by equation (13), the PSPD must exhibit an ideal performance, which requires the application of a reverse bias voltage (V_r) to the PSPD [21]. V_r is often used for improving the time response of a photodiode. However, it is not widely known that the application of V_r is also helpful for increasing the sensitivity (S_z) and decreasing the voltage noise (n_v) as shown in figure 8(a). As a result, n_z decreases with increasing V_r as shown in figure 8(b).

With these improvements, it has become possible to achieve the shot-noise-limited performance even in liquid. Now that the shot noise limit has been achieved, equation (13) gives a direct guideline for the design of low-noise OBD sensors. The major difficulty in the design at this stage is the trade-off between the applicable range of the cantilever dimensions and the noise performance. Among the parameters in equation (13), a_0 and ℓ_f are closely related to this issue (figure 9). A larger a_0 or a shorter ℓ_f results in a smaller laser spot and allows the use of a smaller cantilever. However, this results in a larger n_{zp} as expected from equation (13).

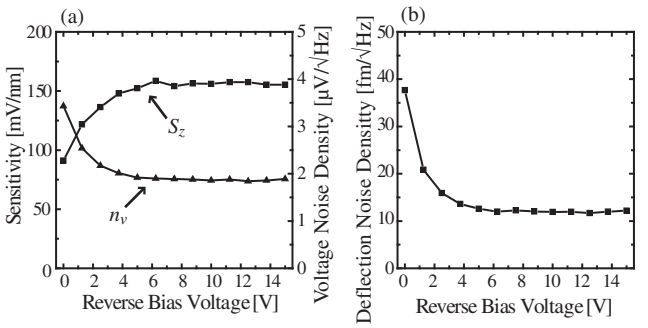

Figure 8. (a) V_r dependence of S_z and n_v. (b) V_r dependence of n_{zs}. The measurements were performed in air. (Reproduced with permission from [26] © 2006 American Institute of Physics.)

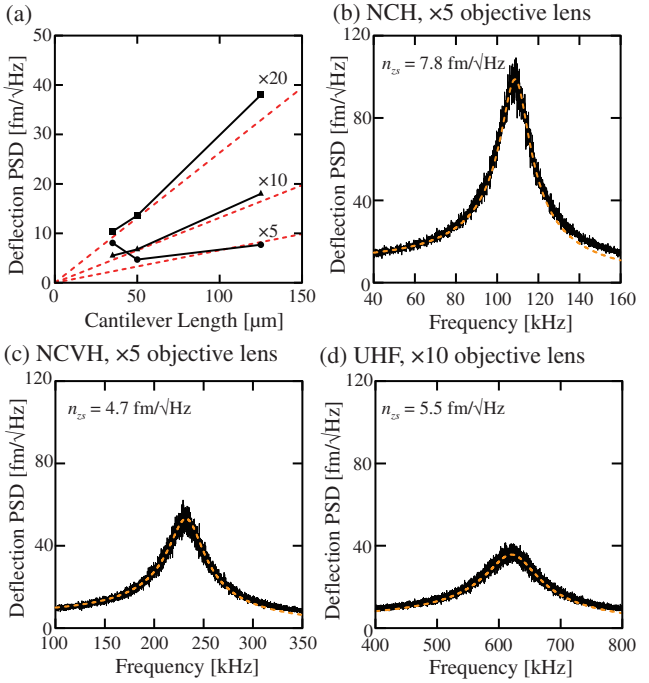

Figure 9. (a) ℓ_c dependence of n_{zs} measured with ×5, ×10 and ×20 objective lenses. The solid lines show experimentally measured values, while the dotted lines were calculated using equation (13). ℓ_f = 10, 20 and 40 mm for ×20, ×10 and ×5 objective lenses, respectively. (b)–(d) Solid lines show the experimentally measured deflection PSD with different cantilevers in water and the dotted lines present the thermally induced deflection PSD calculated using equation (6). (b) Non-contact/tapping mode—high resonance frequency (NCH) cantilever (ℓ_c = 125 μm), ×5 objective lens. (c) Non-contact/tapping mode—very high resonance frequency (NCVH) cantilever (ℓ_c = 50 μm), ×5 objective lens. (d) Ultra-high frequency (UHF) cantilever (ℓ_c = 35 μm), ×10 objective lens. (Reproduced with permission from [21] © 2009 American Institute of Physics.)

One of the possible solutions to this problem is to make the focusing lens replaceable. To implement this idea, the author and his co-workers employed a replaceable objective lens system [21, 26]. As objective lenses of the same series have the same parfocal length, one objective lens can be easily replaced with another without changing the vertical position of the objective lens. A high-magnification lens is used for a small cantilever while a low-magnification lens is used for a

long cantilever. In this way, it is possible to design an OBD sensor that gives the optimal noise performance determined only by the Q factor in liquid.

4. Applications of FM-AFM

4.1. Historical background

The Q factor of the cantilever resonance is much higher in vacuum than in air. The high Q factor in vacuum gives a high SNR in force measurements by dynamic-mode AFM. To take advantage of this benefit, FM-AFM was invented in 1991 to operate dynamic-mode AFM in vacuum [5]. Owing to this historical background, most researchers found no benefits or had no interest in using FM-AFM in liquid, where the Q factor is much smaller than that in air.

In addition, the stable operation of FM-AFM in liquid was expected to be very difficult. FM-AFM requires self-oscillation of the cantilever using the slope in the phase versus distance curve. As the slope changes in proportion to the Q factor (equation (5)), it was expected that stable self-oscillation would be very difficult in liquid.

At this stage, the only clear advantage of using FM-AFM in liquid seemed to be the capability of quantitative and independent measurements of conservative and dissipative forces. In FM-AFM, the cantilever is oscillated at its resonance frequency, where ϕ is kept at -90°. Thus, conservative and dissipative forces independently contribute to Δf and an increase of A_{exc}, respectively. In 2000, Jarvis *et al* started pursuing this possibility. Through the magnetic excitation of the cantilever and the use of a carbon nanotube tip, they obtained Δf and A_{exc} versus distance curves at the interface between highly oriented pyrolytic graphite (HOPG) and octamethylcyclotetrasiloxane (OMCTS) [29]. While the obtained Δf curve showed a monotonic increase, the A_{exc} curve was oscillatory, indicating the structuring of the OMCTS molecules confined between the tip and the HOPG surface.

That pioneering work showed the capability of FM-AFM to visualize the force profile related to the structuring of solvent molecules. Such solvation force measurements had already been demonstrated by static-mode AFM [30]. However, a force curve obtained by static-mode AFM is discontinuous and fails to represent the true continuous oscillatory profile. A short-range attractive force with a large gradient is induced by the structuring of the solvent molecules, leading to jump-to-contact (equation (11)). As a result, 1D-SFM spectroscopy in static-mode AFM cannot visualize the true force profile in the whole tip-sample distance range. In contrast, the A_{exc} curve obtained by FM-AFM showed a continuous oscillatory profile owing to the high stiffness of the cantilever.

The major problem of liquid-environment FM-AFM at this stage was the stability. As the frequency detectors and self-oscillation controllers used for operating FM-AFM were not available, researchers had to develop them in the lab. Because of the instabilities, it was very difficult to scan the tip laterally while maintaining the tip–sample distance based on the Δf signal. Thus, Jarvis *et al* had to use an A_{exc} signal for the feedback in 2D-SFM imaging [29].

In the meantime, sophisticated frequency detectors using analog [31] and digital [32] PLL circuits were being developed primarily for operation in vacuum. In particular, Dürig *et al* proposed the use of the output signal of the voltage-controlled oscillator (VCO) in the PLL circuit as the cantilever excitation signal [31]. In the setup, the PLL works as a band-pass filter with the center frequency tuned to the cantilever resonance. Although this does not necessarily improve the ultimate noise performance of FM-AFM, it helps improve the stability of the FM-AFM operation, especially in liquid where the Q factor is very low.

In 2001, Jarvis *et al* recorded Δf and A_{exc} curves showing oscillatory profiles at the interface between a self-assembled monolayer and OMCTS [33]. They used a custom-built PLL circuit based on the design presented by Dürig *et al* [31]. In 2002, Kobayashi *et al* obtained a 2D-SFM image of an Au(111) surface using tip-sample distance control based on the Δf signal [34] in their custom-built analogue PLL circuit [35]. In 2003, Okajima *et al* also developed a custom-built self-oscillation circuit and an analog PLL circuit to operate FM-AFM in liquid; they compared the amplitude and frequency curves measured at a solid/liquid interface [36]. Using the same system, Sekiguchi *et al* obtained FM-AFM images of protein assemblies on mica in liquid; they controlled the tip–sample distance using the Δf signal [37]. Although at that stage the FM-AFM images obtained in liquid could not show any clear advantages over those obtained by other operation modes, such as contact mode and amplitude modulation (AM) mode, these studies demonstrated the possibility of FM-AFM operation in liquid in both 1D- and 2D-SFM modes.

In addition to the development of instruments, the theoretical understanding of FM-AFM also advanced in the same period. To obtain a quantitative force profile, an experimental Δf versus distance curve must be converted to an F_{t} versus distance curve. Thus, considerable effort was devoted to understanding the relationship between Δf and F_{t}. In 2001, Giessibl presented an intuitive formula showing the relationship between Δf and F_{t} as described by equation (2) [11]. He also presented a simple method for converting Δf data to F_{t} data, where a conversion matrix is first calculated and then multiplied by the Δf values [11]. In 2004, Sader and Jarvis presented a simple analytic formula for force conversion (equation (3)) by mathematically solving the inverse problem starting from equation (2) [12].

Owing to the development of sophisticated PLL circuits dedicated to FM-AFM operation and a simple analytic formula for force conversion, it became possible to obtain a quantitative force versus distance dependence even at a solid/liquid interface. Uchihashi *et al* reported a force versus distance curve obtained in water showing an oscillatory profile with the average peak spacing corresponding to the size of a water molecule [38]. Higgins *et al* presented a force curve showing unbinding events of ligand and receptor molecules [39]. They also obtained force curves showing an oscillatory profile on a lipid bilayer formed on mica in buffer solution [40].

At this stage, the main problem in the application of FM-AFM was the SNR of the force measurement. The experimental Δf versus distance curves showed large noise compared with the variation of Δf corresponding to the oscillatory peaks. In addition, in the force conversion formula (equation (2)), Δf data is differentiated, which further reduces the SNR. To analyze the oscillatory behavior of the peaks, the Δf data was heavily averaged before differentiation and the statistical parameters estimated from a number of averaged force curves were analyzed. Eventually, it was difficult to ensure the accuracy and reliability of the measurement. This problem was particularly serious for a solid/water interface, where the peak spacing of the oscillatory profile (typically 0.2–0.3 nm) is much shorter than that measured at a HOPG/OMCTS interface (typically 0.7–0.8 nm). The low SNR was an even more serious problem in 2D-SFM imaging. In 2D-SFM, the noise in the Δf signal hinders stable control of the tip–sample distance. Thus, stable 2D-SFM imaging is much more difficult than stable 1D-SFM force measurements.

The operating conditions for obtaining the optimal SNR in force measurements by FM-AFM had been discussed at an earlier stage, for operation in vacuum. In 1999, Giessibl *et al* showed that the optimal SNR is obtained with an oscillation amplitude on the order of the decay length of the interaction force [27]. In 2000, Giessibl also pointed out the necessity of using a stiff cantilever for preventing jump-to-contact when operating FM-AFM at a small oscillation amplitude [28]. Giessibl *et al* demonstrated the capability of imaging subatomic-scale structures by oscillating a relatively stiff quartz sensor ($k = 1800\,\mathrm{N\,m^{-1}}$) with a small amplitude ($A = 0.8$ nm) [41]. Although the origin of the subatomic-scale contrasts was disputed, the results clearly demonstrated the benefit of using a small oscillation amplitude.

For applications in vacuum, the main benefit of using a small amplitude is not the improved SNR but the enhanced sensitivity to the short-range interaction force. By oscillating the cantilever with a smaller oscillation amplitude, the tip apex can interact with the surface atom for a longer time, resulting in higher sensitivity to the short-range interaction force and lower sensitivity to the long-range interaction force. As Δf is measured with a finite detection limit, the ratio between the contributions from the short- and long-range forces is crucial in determining the spatial resolution of FM-AFM.

At this stage, there was another important trend toward pursuing imaging with the true atomic and molecular resolution in moderate vacuum or under ambient conditions, which was triggered by several factors. Firstly, there was increasing social demand for applying advanced nanotechnology to the development of industrial material technologies. This required the operation of FM-AFM in air or liquid. Secondly, there was increasing academic interest in the minimum Q factor that allows true atomic-resolution imaging. Finally, the number of FM-AFM users was not increasing rapidly, in spite of the major advances in its performance and the impressive results demonstrated in vacuum. One of the major reasons for this was the lack of a manageable FM-AFM apparatus with true atomic resolution on the market. In this respect, even the development of moderate-vacuum FM-AFM apparatus with true atomic resolution was expected to dramatically expand the application area of FM-AFM.

Motivated by these ideas, some researchers with considerable experience of FM-AFM instrumentation and applications in ultrahigh vacuum started developing FM-AFM apparatus for operation in a low-Q environment. In 2002, Kobayashi *et al* obtained FM-AFM images showing rows of copper phthalocyanine molecules in air [34]. In 2004, Sasahara *et al* recorded FM-AFM images of atomic chains on a TiO_2 surface in N_2 atmosphere [42]. These results suggested that the performance of FM-AFM in ambient conditions at that stage was sufficient for resolving molecular rows but not individual atoms. These results would have been promising if the performance of FM-AFM was limited by the noise from the instruments. In contrary, if it was limited by the Q factor of the environment, these results would have been negative. To clarify this point, the author carried out a detailed noise analysis of FM-AFM instruments and found that the noise from the cantilever deflection sensor can limit the performance of FM-AFM [6]. In 2005, with the developed low-noise cantilever deflection sensor, the author obtained molecularly resolved FM-AFM images of an alkanethiol self-assembled monolayer and a polydiacetylene single crystal in air and in moderate vacuum [43].

After this achievement, the author continued to pursue atomic-resolution imaging with an even lower Q factor, namely, in liquid. At that time, the benefit of using a small oscillation amplitude was becoming accepted and it was natural to examine the performance resulting from small-amplitude oscillation in liquid. For oscillating the cantilever with a small amplitude in vacuum, Giessibl proposed the use of a quartz sensor with stiffness as high as $1800\,\mathrm{N\,m^{-1}}$ to reduce instabilities [28, 41]. However, in an aqueous environment, van der Waals and electrostatic forces are mostly screened by water. Hence, the cantilever stiffness required to reduce the instabilities (equation (11)) should be much lower than that for operation in vacuum—this should partially compensate the disadvantage arising from the low Q factor in liquid. Based on this idea, the author used a cantilever with a spring constant of $40\,\mathrm{N\,m^{-1}}$. From equation (10), this spring constant gives a thermal vibration amplitude of approximately 10 pm, which is just sufficient for obtaining true atomic- and molecular-resolution images.

In 2005, using a cantilever with a spring constant of $40\,\mathrm{N\,m^{-1}}$ and an oscillation amplitude of less than 1 nm with the low-noise cantilever deflection sensor [6], the author obtained molecularly resolved images of a polymer crystal [7] and atomically resolved images of mica [8] in water (figure 10). Although this development was carried out mainly for high-resolution 2D-SFM imaging, the improved stability and force sensitivity also solved the main problems in 1D-SFM experiments. The author and his co-workers obtained low-noise force versus distance curves with piconewton sensitivity at the mica/water interface [8]. Owing to the low-noise cantilever deflection sensor, stable

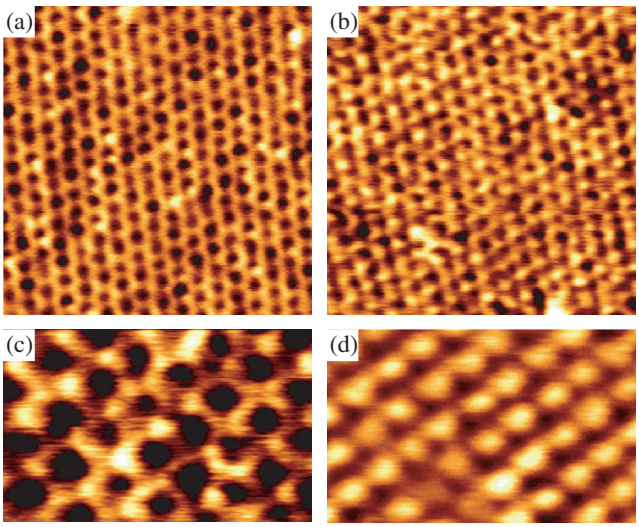

Figure 10. The first atomic-resolution FM-AFM images obtained in liquid. FM-AFM images of the cleaved (001) surface of muscovite mica taken in water. (a) 8 nm ×8 nm, ($f = +54$ Hz, $A = 0.24$ nm, scanning speed: 671 nm s^{-1}; (b) 8 nm × 8 nm, $\Delta f = +240$ Hz, $A = 0.20$ nm, scanning speed: 1120 nm s^{-1}; (c) 4 nm × 2.5 nm, $\Delta f = +157$ Hz, $A = 0.16$ nm, scanning speed: 934 nm s^{-1}; (d) 4 nm × 2.5 nm, $\Delta f = +682$ Hz, $A = 0.20$ nm, scanning speed: 671 nm s^{-1}. The images were taken in constant-height mode, using an n-Si cantilever (Nanosensors: NCH) with a spring constant of 42 N m^{-1} and a resonance frequency of 136 kHz in water. (Reproduced with permission from [8] © 2005 American Institute of Physics.)

self-oscillation with an oscillation amplitude smaller than the size of a water molecule was realized. This condition turned out to be essential for the accurate measurement of an oscillatory force profile presented by hydration layers.

This progress of FM-AFM performance in liquid triggered subsequent FM-AFM applications in biology and electrochemistry using a low-noise cantilever deflection sensor. The author and his co-workers presented molecular-resolution images of lipid bilayers [40], hydration layers [9], lipid-ion networks [44], amyloid fibrils [45], bacteriorhodopsins [46] and GroELs [46] in liquid. The enhancement of FM-AFM performance with a low-noise cantilever deflection sensor was soon confirmed by other research groups. Hoogenboom *et al* presented an atomic-scale image of mica obtained in water and molecular-resolution images of bacteriorhodopsins in buffer solution [47] using a low-noise interferometer [48]. Kawakatsu and co-workers also obtained an atomic-scale images of mica in water [49] using a low-noise Doppler interferometer [50].

Among these applications, the imaging of hydration layers [9] and lipid-ion networks [44] are of particular importance. These results showed that FM-AFM is capable of visualizing not only the structure of a solid surface but also the distribution of mobile molecules and ions interacting with the surface. This idea stimulated the author to develop 3D-SFM for visualizing the complete 3D force field at a solid/water interface [4]. The rest of this section gives an overview of these key applications.

4.2. 1D- and 2D-SFM at lipid/water interface

Water molecules in the vicinity of a biological membrane play an important role in various biological processes. The water molecules interact with the biomolecules constituting the membrane, forming an inhomogeneous distribution at the membrane/water interface. Such hydration layers present energy barriers to approaching solvated ions and proteins. This affects important biological processes such as membrane transport, protein trafficking, signal transduction, membrane fusion and aggregation processes.

The force originating from the water distribution at a membrane/water interface has been intensively studied by various methods owing to its importance in biological processes. It is well known that the physiological environment is very crowded. The distance between opposing biological membranes is often on the order of several water molecules. In such a confined space, water molecules behave differently than in the bulk, and therefore the forces acting between the opposing membranes cannot be predicted by Deryagin–Landau–Verwey–Overbeek (DLVO) theory. The inter-membrane interactions are also important in biological processes where membrane–membrane, vesicle–vesicle and vesicle–membrane interactions are involved.

The force acting between two opposing membranes has been measured by surface force apparatus (SFA) [51] and the osmotic stress method [52–54]. The results obtained by both methods indicated that the force increases exponentially with decreasing distance between membranes below 1 nm. Because of the agreement of the decay length with the size of a water molecule, the force was attributed to the interaction mediated through the hydration layers formed on the membrane surface.

However, it was unclear whether the force actually originated from the intrinsic hydration layers at the lipid/water interface. Furthermore, even the existence of hydration layers has also been questioned. For one reason, it was proposed that the repulsive force originates from the steric repulsion between lipid molecules [55, 56]. In the proposed model, lipid molecules show large fluctuation in the vertical direction, which hinder the formation of a stable hydration layer. The protrusion of individual molecules caused by thermal fluctuations results in a repulsive force that monotonically increases with decreasing distance between the membranes.

It is well known that the force acting between two opposing flat surfaces (e.g. mica) shows an oscillatory dependence on the distance between them owing to the layering of the confined water molecules [57]. Thus, the monotonic variation of the force between the two opposing membranes was considered as evidence for the nonexistence of hydration layers.

One of the major difficulties in such investigations was the lack of a method to visualize the water distribution at the solid/water interface with molecular-scale spatial resolution. In the osmotic stress method and SFA measurements, the local force profiles were averaged over a micrometer-scale area. It was therefore difficult to determine the molecular-scale origin of the measured force profile. Molecular dynamics simulations suggested the existence of local hydration shells around individual lipid molecules [58]. Such local oscillatory

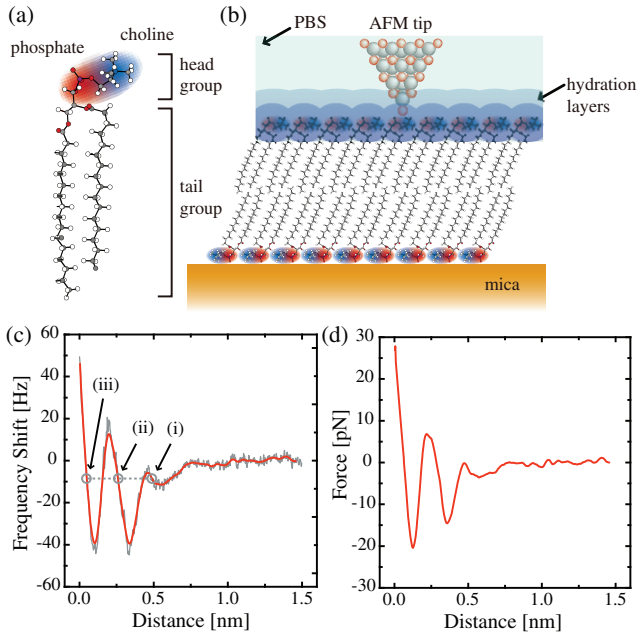

Figure 11. (a) Model of DPPC molecules. (b) Model of a DPPC bilayer with an AFM tip in phosphate buffer saline (PBS) solution. (c) Example of Δf versus distance curve measured on a DPPC bilayer in PBS solution showing an oscillatory profile with two peaks. The smoothed line is obtained by averaging the raw data over the distance range of ± 0.02 nm at each data point. (d) Force versus distance curve converted from (a) using equation (3). (Reproduced with permission from [9] © 2007 Biophysical Society.)

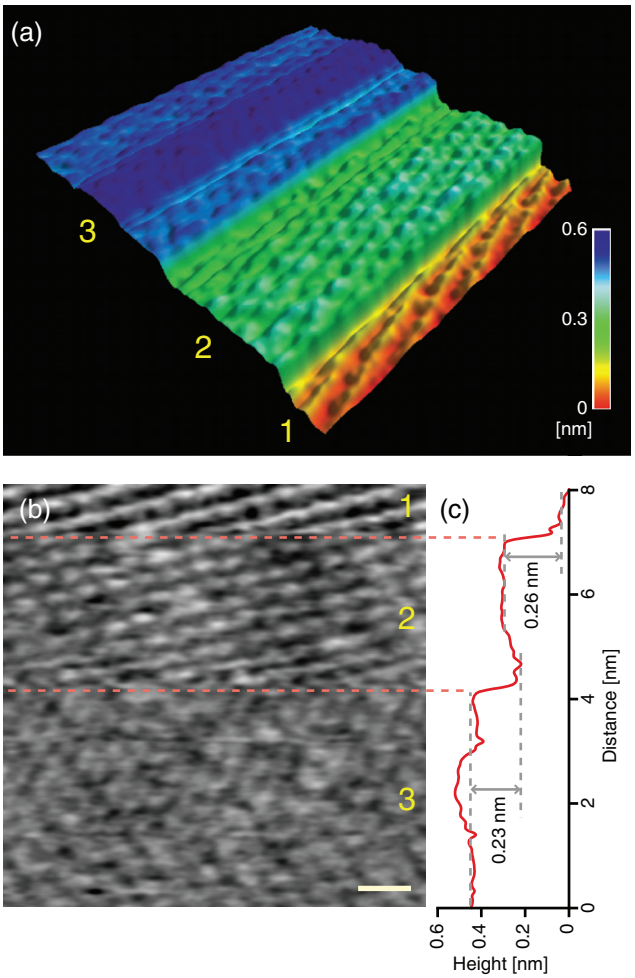

Figure 12. (a) FM-AFM image of the DPPC bilayer in PBS solution showing spontaneous jumps during the imaging. Scan range: 8 nm × 8 nm, tip velocity: 120 nm s^{-1}, imaging speed: 85 s $frame^{-1}$. (b) Line-by-line flattened image of (a). Scale bar: 1 nm, height range: 0.1 nm (black to white). Fast and slow scan directions: left to right and top to bottom, respectively. The regions indicated by numbers 1, 2 and 3 correspond to terraces 1, 2 and 3 in (a). (c) Line-averaged height profile of (b) plotted along the slow-scan direction. (Reproduced with permission from [9] © 2007 Biophysical Society.)

force profiles may be smeared out by global averaging due to the undulation and roughness of the soft lipid membrane.

1D-SFM is an ideal tool for investigating local interaction forces. As the apex of an AFM tip has a nanoscale cross section, the force acting on the tip during its approach to a membrane surface should be similar to the local forces that biomolecules experience when they approach the membrane surface (figure 11(b)).

Figure 11(c) shows a Δf versus distance curve measured on a dipalmitoylphosphatidylcholine (DPPC) bilayer in PBS solution [9]. Using equation (3), the Δf curve was converted to a quantitative force curve as shown in figure 11(d). The force curve has an oscillatory profile with two peaks. The distance between the peaks is 0.25 nm, which roughly corresponds to the size of a water molecule. This suggests that the oscillatory force profile originates from the hydration layers formed on the DPPC bilayer.

The previously reported force curves obtained by SFA and the osmotic stress method showed a monotonic increase with distance [51–54], whereas 1D-SFM (figure 11(d)) revealed an oscillatory profile. The latter result supported the model where hydration layers locally exist on a lipid bilayer and their oscillatory force profiles are smeared out when they are averaged over a micrometer-scale area.

The Δf curve in figure 11(c) shows almost no influence from the long-range interaction force. The contribution from the long-range force strongly depends on the conditions of the tip, sample and especially the solution. In particular, the increase of the salt content in the solution tends to suppress the long-range interaction owing to the reduction of the Debye length. The fluctuations of the molecules constituting the surface are considered to increase the long-range interaction force. In this experiment, the solution contained approximately 150 mM NaCl and the DPPC molecules were in the stable gel phase. Under these experimental conditions, the effect of the long-range interaction force on the observed Δf curve should be small.

In 2D-SFM, the feedback control of the vertical tip position is based on the assumption that Δf increases as the tip approaches the surface. Thus, the oscillatory force profile at a solid/liquid interface results in the existence of multiple feedback positions as indicated by the arrows (i)–(iii) in figure 11(c). During the scan, the tip may jump between these feedback positions even if the set point for feedback regulation is unchanged. An example of such 2D-SFM imaging is shown in figure 12.

In the 2D-SFM image (figure 12), the tip is scanned from the lowest terrace (terrace 1), which corresponds to the surface of the DPPC bilayer. The image shows molecular-scale corrugations corresponding to individual head groups. During the scan, the tip jumped from terrace 1 to terrace 2. The height of the jump is 0.26 nm. This value corresponds to the size of a water molecule, suggesting that terrace 2 corresponds to the interface between the primary and secondary hydration layers. In the image, molecular-scale corrugations are still visible. This means that the primary hydration layer has a nonuniform lateral distribution that reflects molecular-scale surface corrugations.

The tip also jumped from terrace 2 to terrace 3 during the scan. The height of the jump was 0.23 nm, which also agrees with the size of a water molecule. Thus, terrace 3 should correspond to the boundary between the secondary hydration layer and the bulk water. The molecular-scale corrugations are still visible in this image although the corrugation height is very small. This result indicates that the molecular-scale corrugations of the membrane surface can influence the water distribution even in the secondary hydration layer.

The results obtained by 1D- and 2D-SFM consistently suggest the existence of stable hydration layers undisrupted by the thermal fluctuations of lipid molecules. These hydration layers extend laterally beyond the nanometer scale. Although the water distribution may be different under other conditions (e.g. ion contents, temperature and molecular species), these results demonstrated that FM-AFM can provide direct molecular-scale information that cannot be obtained by conventional techniques.

4.3. 3D-SFM at mica/water interface

It is possible to analyze the 3D water distribution from the results obtained by 1D- and 2D-SFM. However, such an analysis is often inefficient and/or inaccurate. For example, in the imaging of hydration layers described above, the jumps between the feedback positions cannot be manually controlled. In fact, the two sequential jumps between the feedback positions observed in the image shown in figure 12 occurred by chance. The author recorded more than a hundred 2D-SFM images, analyzed them and selected one of the few images showing sequential jumps. Even for a simple system such as a lipid bilayer, the experiment and analysis were inefficient. Thus, it is not practical to apply this methodology to more complicated systems consisting of various biomolecules.

To resolve this issue, we have developed 3D-SFM, which is capable of visualizing the 3D force field at a solid/liquid interface. Any 1D force profile or 2D force image can be extracted from the 3D force image. The process of extraction and analysis effectively replaces the experiment and analysis in conventional 1D- and 2D-SFM. As the first application of the developed 3D-SFM, the author and his co-workers investigated the mica/water interface, which highlights the benefits of 3D-SFM.

Muscovite mica is known as a prototype of clay minerals and hence is important in fundamental research on clay

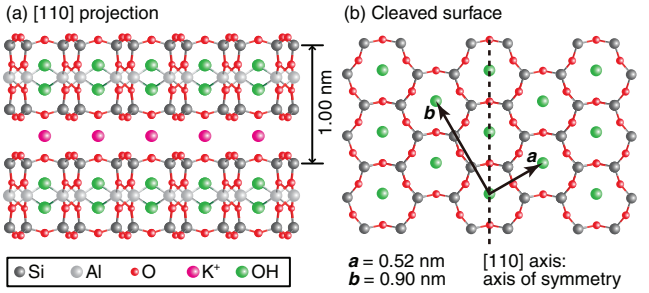

Figure 13. Crystal structure of muscovite mica $[KAl_2(Si_3Al)O_{10}(OH)_2]$ [59]. (a) [110] projection. (b) Cleaved surface. (Reused with permission from [4] © 2010 American Physical Society.)

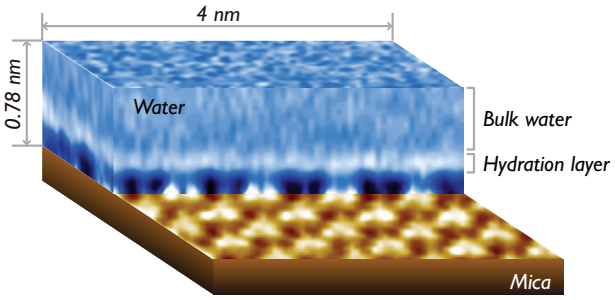

Figure 14. 3D-SFM image obtained at the interface between a cleaved mica surface and PBS solution ($A = 0.62$ nm). The 3D-SFM image ($4 \times 4 \times 0.78$ nm^3) was constructed from approaching Z profiles and has $64 \times 64 \times 155$ pixels. The frequency and amplitude of the Z modulation during 3D-SFM imaging were 200 Hz and 0.78 nm, respectively. The lateral scan speed was 12.2 nm s^{-1}. Each XZ cross-sectional image was obtained within 0.32 s while the whole 3D image was obtained within 53 s.

swelling in geology [60–62] and cloud seeding in ecology [63, 64]. Furthermore, cleaved mica presents an atomically flat surface as shown in figure 13. Thus, the mica/water interface has been widely used as a platform for studies on nanofluidics in engineering and physics [65], lubrication in tribology, and molecular adsorption and diffusion in biology and chemistry. The water distribution at the mica/water interface has been extensively studied by various techniques [1, 66–71]; however, an atomic model of the interface has not been established owing to difficulties in visualizing the distribution of individual water molecules at the solid/liquid interface.

The author and his co-workers obtained a 3D-SFM image of the mica/water interface as shown in figure 14. Owing to the simple motion of the tip in 3D-SFM, the whole 3D image was recorded with atomic-scale resolution within only 53 s. This capability of fast imaging is essential to avoid image distortions induced by nonlinear tip drift. Even at this imaging speed, we could not eliminate linear drift. Thus, we applied linear drift compensation to the 3D image in figure 14 and its cross sections, which are presented in figures 15 and 16, respectively.

Once the complete 3D force field is obtained, it is possible to extract any 1D profile or 2D cross section. An XY-averaged force curve was obtained by plotting the force values averaged over an XY cross section at each z_t

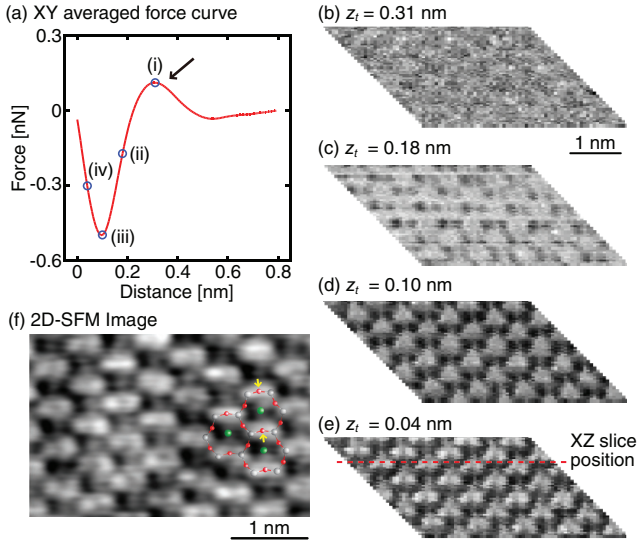

Figure 15. 3D- and 2D-SFM images of mica/water interface obtained in PBS solution. (a) *XY*-averaged force curve. The position of $z_t = 0$ is arbitrary. (b)–(e) *XY* cross sections of the 3D-SFM image at $z_t = 0.31$, 0.18, 0.10 and 0.04 nm, which respectively correspond to the z_t positions indicated by circles (i)–(iv) in (a). A linear drift correction was applied to the *XY* cross sections so that the periodic contrast matches the known lattice constants of a cleaved mica surface. The dotted line in (e) indicates the *Y* position of the *XZ* cross section shown in figure 16(a). (f) 2D-SFM image ($A = 0.26$ nm, $\Delta f = 67.1$ Hz) obtained with a different tip from the one used for the 3D-SFM imaging. (Reproduced with permission from [4] © 2010 American Physical Society.)

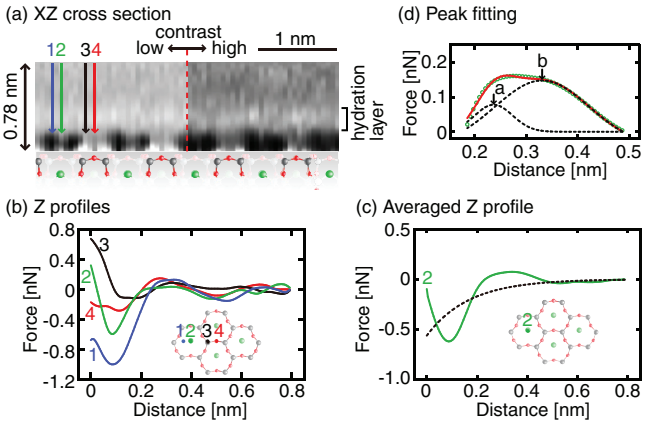

Figure 16. *XZ* cross section and *Z* profiles of a 3D-SFM image of a mica/water interface in PBS solution. (a) *XZ* cross section obtained at the *Y* position indicated by a dotted line in figure 15(e). An atomic-scale model of the [110] projection of muscovite mica is shown below the *XZ* cross section. (b) *Z* profiles measured along lines 1–4 in (a). (c) Average of 48 *Z* profiles measured at the OH sites. The dotted line is an exponential fit. The insets in (b) and (c) show the measurement positions for the *Z* profiles. (d) The circles show the peak profile obtained by subtracting the dotted line in (c) from the solid line in (c). The dotted lines show the double Gaussian peak profiles obtained by fitting the peak profile; z_t values for peaks *a* and *b* are 0.237 and 0.331 nm, respectively. The solid line is the sum of the two dotted lines. (Reproduced with permission from [4] © 2010 American Physical Society.)

(figure 15(a)). This curve shows an oscillatory profile with a peak (arrow in figure 15(a)) width of 0.2–0.3 nm, which agrees with the size of a water molecule. Owing to this agreement and previous studies on mica/water interfaces [8, 72], the peak was attributed to the interaction with a hydration layer.

From the *XY* cross sections at different z_t (figures 15(b)–(e)), a continuous z_t dependence of the *XY* force is obtained. The *XY* cross section in figure 15(b) does not show any contrast variations. This means that the water molecules have a uniform lateral distribution in the hydration layer. As the tip approaches the surface, the *XY* cross section shows an atomic-scale contrast (figures 15(c)–(e)), reflecting the short-range interaction between the front atoms of the tip and those of the mica surface. With a further decrease of z_t, the hexagonally arranged force peaks found in figure 15(d) changed to pairs of smaller peaks (figure 15(e)).

The periodic pairs of force peaks found in figure 15(e) appear to be uniform, which leads to the question of whether the contrast represents the structure of the mica surface or that of the tip apex [41]. However, a similar contrast is reproduced in the 2D-SFM image obtained with a different tip as shown in figure 15(f). The image shows the irregular variation in the height of individual atoms, suggesting that the contrast is unlikely to be due to a tip artifact. By comparing the image of figure 15(f) and the atomic-scale model of mica (figure 13(b)), we attributed the pairs of force peaks to the repulsive forces between the two adjacent Si atoms, as indicated by the model overlaid on the image of figure 15(f).

Both the 3D- and 2D-SFM images show an atomic-scale contrast with mirror symmetry. This is an important finding because a cleaved mica surface is often postulated to have sixfold symmetry. Strictly speaking, this is inaccurate. The atomic-scale model derived from x-ray diffraction data [59] shows that a cleaved mica surface does not have a sixfold but mirror symmetry as shown in figure 13(b). However, this feature found in the SFM images is more evident than expected from the atomic-scale model. This is because two of the six oxygen atoms constituting the hexagonal ring, which are indicated by arrows in figure 15(f), are imaged with a brighter contrast than the other four atoms. Such a difference from the atomic-scale model obtained with a bulk crystal suggests surface relaxation at the mica/water interface.

Another feature found in the SFM images is an enhanced contrast at the center of the cavity surrounded by a hexagonal ring. The overlaid model shown in figure 15(f) shows that the *XY* position of the enhanced contrast agrees with that of an OH group located at the bottom of the cavity. Even for an atomically flat surface such as mica, there are atomic-scale height corrugations. They complicate the analysis of the correlation between the atomic-scale structure and the force distribution obtained from a 2D-SFM image, which has no vertical extent. Such an analysis on the vertical distribution of water becomes possible by extracting a vertical cross section from a 3D-SFM image as shown in figure 16(a). The left half of the *XZ* cross section is shown with a low contrast to visualize the localized force distribution above an OH group, whereas the right half has a high contrast to accentuate the layer-like force distribution over the entire surface. The latter distribution corresponds to the repulsive peak indicated by the arrow in figure 15(a).

By extracting individual Z profiles constituting the XZ cross section, site-specific force curves were obtained as shown in figure 16(b). The Z profiles show strong site dependence, particularly when $z_t < 0.2$ nm. Profile 1 shows a large attractive force owing to the absence of an underlying atom. Profile 2 has a relatively broad repulsive peak owing to the localized force distribution above an OH group. In contrast, profile 3 has a shallow and broad attractive peak due to the competition between the attractive van der Waals or hydration force and a repulsive interaction force between the tip and the Si atom. This means that the repulsive-force component measured on the Si site starts to increase at a higher z_t than it does on the OH site, reflecting their height difference.

In spite of the similar Z positions of Si and oxygen atoms, profiles 3 and 4 exhibit markedly different features. Profile 4 does not present a repulsive-force branch but an almost constant force for the Z distance range of $z_t = 0$ to -0.15 nm. At a cleaved mica surface, a Si atom is strongly supported by four tetrahedrally arranged chemical bonds, whereas an oxygen atom is supported by only two chemical bonds, giving it greater flexibility. Therefore, the repulsive force between an oxygen atom and the approaching tip may be strong enough to displace oxygen, accounting for the constant-force regime observed in profile 4.

Profile 2 shows a relatively broad repulsive peak owing to the localized force distribution above an OH group. To analyze the peak profile, 48 Z profiles measured on OH sites were extracted from the 3D-SFM image and averaged to obtain the smoothed curve of figure 16(c). The averaged curve was fitted with an exponential function to obtain a long-range background component indicated by the dotted line in figure 16(c). This long-range component was subtracted from the averaged force profile to obtain the peak profile shown in figure 16(d). The peak presents a broad profile with a plateau, which appears as a double peak. We fitted the peak profile with the two Gaussians indicated by dotted lines in figure 16(d). The smaller peak at $z_t = 0.237$ nm (peak a) has a width of 0.103 nm and the major peak at $z_t = 0.331$ nm (peak b) has a width of 0.258 nm.

So far, some of the previous studies of the mica/water interface have supported the existence of 'ice-like' water [66–68] whereas others have suggested a more disordered 'liquid-like' water structure [69, 70]. Recently, x-ray reflectometry [1] and Monte Carlo simulation [71] results have consistently suggested the existence of adsorbed water molecules presenting localized water distribution above the OH groups in addition to a laterally distributed hydration layer. The water density profiles obtained in these previous studies revealed that the Z distance between the peaks corresponding to the hydration layer and the adsorbed water molecules is 0.12 nm. This value approximately agrees with the peak distance (0.094 nm) measured in figure 16(d), which suggests that the enhanced contrast measured on the OH sites should represent the localized distribution of adsorbed water molecules. Therefore, the results obtained in this study support the model proposed by Cheng *et al* [1], where the adsorbed and laterally distributed water molecules coexist at the interface. The coexistence of water molecules having a long relaxation time (adsorbed water) and laterally distributed disordered water molecules (2D hydration layer) may reconcile the two ideas of ice-like and liquid-like water molecules at the mica/water interface.

Comparing the 3D-SFM investigation of the mica/water interface with the 1D- and 2D-SFM studies of the lipid/water interface, one can clearly understand the benefits of having a complete 3D force field. For the 1D force profiles shown in figure 11, the XY position is not known except that the curve was measured on the DPPC bilayer. Theoretically, it is possible to obtain a 2D-SFM image and take a force curve at a specific XY position. Indeed, this method has often been used for imaging in vacuum. However, in liquid-environment experiments, nonlinear tip drift often exists due to the swelling of the cantilever holder, the tip holder and the substrate. Evaporation of the liquid can also induce nonlinear drift. The nonlinear drift prevents the accurate control of the XY position with atomic-scale precision. In contrast, the 1D profiles shown in figure 16(b) were extracted from the 3D-SFM image so that the XY position of the Z profile is well defined with atomic-scale precision.

Another benefit of 3D-SFM is the improved efficiency. The 2D height image shown in figure 12 was obtained by analyzing more than a hundred images, whereas the 2D force images shown in figure 15 were obtained by extracting cross sections from the 3D-SFM image. More importantly, in 2D-SFM there are Z positions where tip-sample distance control does not work (e.g. (i) and (iii) indicated in figure 15(a)). Thus, 2D-SFM can provide only limited information on the 3D interfacial space. In 3D-SFM, the Z position for the extraction of an XY cross section can be accurately and arbitrarily determined as demonstrated in figure 15. These features provide enhanced efficiency and accuracy in the investigation of solid/water interfaces.

5. Summary and future prospects

The force sensitivity and spatial resolution of FM-AFM in liquid have remarkably advanced in the last decade, enabling the visualization of 1D profiles of the hydration force, 2D images of hydration layers and 3D distributions of water molecules. At present, FM-AFM studies on solid/liquid interfaces are rather limited in number. However, considering the large number of scientific fields and industrial technologies related to solid/liquid interfaces, I am convinced that the number of FM-AFM applications in this area will grow rapidly in the near future.

Important issues must be solved to continue this progress. First of all, the operation speed of FM-AFM is often insufficient for its operation in liquid. The author has imaged various samples by liquid-environment FM-AFM, and in most cases this problem was evident. For example, in the imaging of an isolated biomolecular system weakly bound to a solid surface (e.g. amyloid fibrils [45]), it was very difficult to avoid removing the molecules from the surface by the tip crash. One solution is to use a soft cantilever; however, this results in a low spatial resolution. A better solution to this problem

is to increase the speed of tip-sample distance regulation. Another example is the imaging of a heterogeneous surface consisting of a complex mixture of various molecules (e.g. multicomponent lipid bilayers [25]). Owing to the complexity, it is often very difficult to understand the whole picture of the surface from the combination of low-resolution images of a large area and high-resolution images of a small area. Ideally, a high-resolution image of a large area should be obtained, but this requires either a long imaging time or fast operation speed. The former solution is not always applicable. For example, in many biological applications, the solution contains various molecules, which inevitably adhere to the cantilever. Chemical modification of the cantilever surface may be effective but only in some cases. Thus, the enhancement of the operation speed should be a more fundamental solution to this problem. In addition, at a solid/liquid interface, the structures, positions and distributions of molecules and ions are often changing during the measurement (e.g. lipid-ion networks [44]). The visualization of such dynamic events also requires faster imaging.

Secondly, further improvement of the force sensitivity is necessary for imaging surface properties by FM-AFM. For example, there has been a trend toward combining FM-AFM with Kelvin probe force microscopy to visualize the surface potential distribution at solid/liquid interfaces. Such a surface measurement often requires higher force sensitivity than that required for topographic imaging. The present FM-AFM instrument has a force sensitivity only as high as that required for topographic imaging. Therefore, improvement of the force sensitivity will be essential for expanding the capability of liquid-environment FM-AFM.

Acknowledgment

This research was supported by PRESTO, Japan Science and Technology Agency.

References

[1] Cheng L, Fenter P, Nagy K L, Schlegel M L and Sturchio N C 2001 *Phys. Rev. Lett.* **87** 156103
[2] Cole D R, Herwig K W, Mamontov E and Larese J Z 2006 *Rev. Miner. Geochem.* **63** 313
[3] Binnig G, Quate C F and Gerber Ch 1986 *Phys. Rev. Lett.* **56** 930
[4] Fukuma T, Ueda Y, Yoshioka S and Asakawa H 2010 *Phys. Rev. Lett.* **104** 016101
[5] Albrecht T R, Grütter P, Horne D and Ruger D 1991 *J. Appl. Phys.* **69** 668
[6] Fukuma T, Kimura M, Kobayashi K, Matsushige K and Yamada H 2005 *Rev. Sci. Instrum.* **76** 053704
[7] Fukuma T, Kobayashi K, Matsushige K and Yamada H 2005 *Appl. Phys. Lett.* **86** 193108
[8] Fukuma T, Kobayashi K, Matsushige K and Yamada H 2005 *Appl. Phys. Lett.* **86** 034101
[9] Fukuma T, Higgins M J and Jarvis S P 2007 *Biophys. J.* **92** 3603
[10] Meyer G and Amer N M 1988 *Appl. Phys. Lett.* **53** 1045
[11] Giessibl F J 2001 *Appl. Phys. Lett.* **78** 123
[12] Sader J E and Jarvis S P 2004 *Appl. Phys. Lett.* **84** 1801
[13] Sader J E, Uchihashi T, Higgins M J, Farrell A, Nakayama Y and Jarvis S P 2005 *Nanotechnology* **16** S94
[14] Hölscher H, Langkat S M, Schwarz A and Wiesendanger R 2002 *Appl. Phys. Lett.* **81** 4428
[15] Ternes M, Lutz C P, Hirjibehedin C F, Giessibl F J and Heinrich A J 2008 *Science* **319** 1066
[16] Albers B J, Schwendemann T C, Baykara M Z, Pilet N, Liebmann M, Altman E I and Schwarz U D 2009 *Nat. Nanotech.* **4** 307
[17] Gross L, Mohn F, Liljeroth P, Repp J, Giessibl F J and Meyer G 2009 *Science* **324** 1428
[18] Martin Y, Williams C C and Wickramasinghe H K 1987 *J. Appl. Phys.* **61** 4723
[19] Jarvis S P, Oral A, Weihs T P and Pethica J B 1993 *Rev. Sci. Instrum.* **64** 3515
[20] Umeda N, Ishizaki S and Uwai H 1991 *J. Vac. Sci. Technol.* B **9** 1318
[21] Fukuma T 2009 *Rev. Sci. Instrum.* **80** 023707
[22] Degertekin F L, Hadimioglu B, Sulchek T and Quate C F 2001 *Appl. Phys. Lett.* **78** 1628
[23] Onaran A G and Degertekin F L 2005 *Rev. Sci. Instrum.* **76** 103703
[24] Carrasco C, Ares P, de Pablo P J and Gómez-Herrero J 2008 *Rev. Sci. Instrum.* **79** 126106
[25] Asakawa H and Fukuma T 2009 *Rev. Sci. Instrum.* **80** 103703
[26] Fukuma T and Jarvis S P 2006 *Rev. Sci. Instrum.* **77** 043701
[27] Giessibl F J, Bielefeldt H, Hembacher S and Mannhart J 1999 *Appl. Surf. Sci.* **140** 352
[28] Giessibl F J 2000 *Appl. Phys. Lett.* **76** 1470
[29] Jarvis S P, Uchihashi T, Ishida T, Tokumoto H and Nakayama Y 2000 *J. Phys. Chem.* B **104** 6091
[30] O'Shea S J, Welland M E and Rayment T 1992 *Appl. Phys. Lett.* **60** 2356
[31] Dürig U, Steinauer H R and Blanc N 1997 *J. Appl. Phys.* **82** 3641
[32] Loppacher Ch, Bammerlin M, Battiston F, Guggisberg M, Müller D, Hidber H R, Lüthi R, Meyer E and Güntherodt H J 1998 *Appl. Phys.* A **66** S215
[33] Jarvis S P, Ishida T, Uchihashi T, Nakayama Y and Tokumoto H 2001 *Appl. Phys.* A **72** S129
[34] Kobayashi K, Yamada H and Matsushige K 2002 *Appl. Surf. Sci.* **188** 430
[35] Kobayashi K, Yamada H, Itoh H, Horiuchi T and Matsushige K 2001 *Rev. Sci. Instrum.* **72** 4383
[36] Okajima T, Sekiguchi H, Arakawa H and Ikai A 2003 *Appl. Surf. Sci.* **68** 210
[37] Sekiguchi H, Okajima T, Arakawa H, Maeda S, Takashima A and Ikai A 2003 *Appl. Surf. Sci.* **61** 210
[38] Uchihashi T, Higgins M J, Nakayama Y, Sader J E and Jarvis S P 2005 *Nanotechnology* **16** S49
[39] Higgins M J, Riener Ch K, Uchihashi T, Sader J E, McKendry R and Jarvis S P 2005 *Nanotechnology* **16** S85
[40] Higgins M J, Polcik M, Fukuma T, Sader J, Nakayama Y and Jarvis S P 2006 *Biophys. J.* **91** 2532
[41] Giessibl F J, Hembacher S, Bielefeldt H and Mannhart J 2000 *Science* **289** 422
[42] Sasahara A, Kitamura S, Uetsuka H and Onishi H 2004 *J. Phys. Chem.* B **108** 15735
[43] Fukuma T, Ichii T, Kobayashi K, Yamada H and Matsushige K 2005 *Appl. Phys. Lett.* **86** 034103
[44] Fukuma T, Higgins M J and Jarvis S P 2007 *Phys. Rev. Lett.* **98** 106101
[45] Fukuma T, Mostaert A S, Serpell L C and Jarvis S P 2008 *Nanotechnology* **19** 384010
[46] Yamada H, Kobayashi K, Fukuma T, Hirata Y, Kajita T and Matsushige K 2009 *Appl. Phys. Express* **2** 095007
[47] Hoogenboom B W, Hug H J, Pellmont Y, Martin S, Frederix P L T M, Fotiadis D and Engel A 2006 *Appl. Phys. Lett.* **88** 193109

[48] Hoogenboom B W, Frederix P L T M, Yang J L, Martin S, Pellmont Y, Steinacher M, Zäch S, Langenbach E and Heimbeck H-J 2005 *Appl. Phys. Lett.* **86** 074101
[49] Nishida S, Kobayashi D, Sakurada T, Nakazawa T, Hoshi Y and Kawakatsu H 2008 *Rev. Sci. Instrum.* **79** 123703
[50] Kawai S, Kobayashi D, Kitamura S, Meguro S and Kawakatsu H 2005 *Rev. Sci. Instrum.* **76** 083703
[51] Marra J and Israelachvili J N 1985 *Biochemistry* **24** 4608
[52] LeNeveu D M, Rand R P and Parsegian V A 1976 *Nature* **259** 601
[53] Lis L J, McAlister M, Fuller N, Rand R P and Parsegian V A 1982 *Biophys. J.* **37** 657
[54] McIntosh T J and Simon S A 1986 *Biochemistry* **25** 4058
[55] Israelachvili J N and Wennerström H 1990 *Langmuir* **6** 873
[56] Israelachvili J N 1992 *Intermolecular and Surface Forces* (London: Academic)
[57] Israelachvili J N and Pashley R M 1983 *Nature* **306** 249
[58] Berkowitz M L, Bostick D L and Pandit S 2006 *Chem. Rev.* **106** 1527
[59] Richardson S M and Richardson J W 1982 *Am. Mineral.* **67** 69
[60] Hochella M Jr and White A F (ed) 1990 *Review in Mineralogy: Mineral Water Interface Geochemistry* (Mineralogical Society of America)
[61] Boek E S, Coveney P V and Skipper N T 1995 *J. Am. Chem. Soc.* **117** 12608
[62] Karaborni S, Smit B, Heidug W, Urai J and van Oort E 1996 *Science* **271** 1102
[63] Edwards G R, Evans L F and Zipper A F 1970 *Trans. Faraday Soc.* **66** 220
[64] Caslavsky J L and Vedam K 1971 *J. Appl. Phys.* **42** 516
[65] Leng Y and Cummings P T 2006 *J. Phys. Chem.* **124** 074711
[66] Sposito G and Prost R 1982 *Chem. Rev.* **82** 553
[67] Odelius M, Bernasconi M and Parrinello M 1997 *Phys. Rev. Lett.* **78** 2855
[68] Miranda P B, Xu L, Shen Y R and Salmeron M 1998 *Phys. Rev. Lett.* **81** 5876
[69] Bergman R and Swenson J 2000 *Nature* **403** 283
[70] Swenson J, Bergman R and Howells W 2000 *J. Chem. Phys.* **113** 2873
[71] Park S-H and Sposito G 2002 *Phys. Rev. Lett.* **89** 085501
[72] Israelachvili J N and Adams G E 1976 *Nature* **262** 774